Biosensors and Bioelectronics 179 (2021) 113081

Contents lists available at ScienceDirect

Biosensors and Bioelectronics

journal homepage: http://www.elsevier.com/locate/bios

Harmonic optical microfiber Bragg grating immunosensor for the accelerative test of cardiac biomarker (cTn-I)

Yang Ran [a], Junqiu Long [a], Zhiyuan Xu [a], Yi Yin [a], Deming Hu [a], Xueting Long [a], Yongkang Zhang [a], Lili Liang [a,b], Hao Liang [a], Bai-Ou Guan [a,*]

[a] Guangdong Provincial Key Laboratory of Optical Fiber Sensing and Communications, Institute of Photonics Technology, Jinan University, Guangzhou, 510632, China
[b] Institute of Information Technology, Handan University, Handan, 056005, China

ARTICLE INFO

Keywords:
Optical microfibers
Harmonic bragg grating
Cardiac troponin I
Acute myocardial infarction diagnosis
Temperature compensation
Test acceleration

ABSTRACT

Fiber-optic biosensor has shown tremendous promise in probing cardiac biomarkers label-free and *in-operando*. However, temperature cross-sensitivity is ubiquitously found and impedes further advances of the fiber-optic biosensors, especially for the scenario of rapid test at-body. In this study, we exploit a new regime that harnesses the harmonic resonances of a single microfiber Bragg grating to rule out the impact of the thermal noise. The reflections yielded by the harmonics can be engineered simultaneously at the two overriding optical wavebands, i.e., 1 μm and 1.55 μm, promising a remote acquisition of the sensing signals at patient by virtue of the Yb and/or Er-doped fiber amplifiers which are highly commercial. Furthermore, the functionality of the temperature-offset allows for the understanding of the biomolecular stimulating at the body temperature and thus facilitating the acceleration of the cardiac biomarker test. The proposed proof-of-concept enriches the arsenal of tools for fiber biosensors and enables a vista for the instant and *in-vivo* diagnosis of acute heart diseases.

1. Introduction

Annually, millions of individuals are hanged over by the shadow of death caused by cardiac diseases (WHO, 2015). As one of the most notorious diseases, acute myocardial infarction (AMI, or heart attack) kills hundreds of thousands of people worldwide and tremendously burdens medical care due to the various high-risk complications. (Thygesen et al., 2012; White and Chew, 2008). Rapid screening is essential to reduce the threat and severity of AMI because it allows for the classification of the risky groups and the specification of the therapeutic schedule as early as possible. Since the level of the specifically cardiac biomarker in the patient blood plays a pivotal character in benchmarking the standard of the screen, the test of the cardiac biomarkers becomes an indispensable build block in the remedy for AMI. (Tripoliti et al., 2020; Fathil et al., 2015; Qureshi et al., 2012; Mahajan and Jarolim, 2011; Mohammed and Desmulliez, 2011).

In contrast with the routine testing approaches involving labeling immunoassay, for example, the enzyme-linked immunosorbent assay (ELISA) and fluorescence immunoassay (Tuteja et al., 2016; Fan et al., 2008), label-free immunosensors promise a fascinating route for the determination of cardiac biomarker without being subjected to the laborious sample labeling and the time-consuming transportation to the central lab. Compared with the electronic-based cardiac marker probe, for example, the quartz crystal microbalance (Agafonova et al., 2014; Mattos et al., 2012)-a useful tool for studying complex biomolecular interaction, label-free optic-based cardiac marker sensor enables the immunity to electromagnetic interference, benefitting for the application in the complex electromagnetic environment. A plethora of photonic and optic transducers was devoted to the cardiac biomarker sensing, including localized surface plasmonic resonance (Tang and Casas, 2014), surface plasmonic resonance (Wu et al., 2017; Pawula et al., 2016), total internal reflection (Zhang et al., 2014), polarized light wave (Diware et al., 2017), surface-enhanced Raman scattering (Zhang et al., 2018a, 2018b; El-Said et al., 2016; Saliminasab et al., 2012) and photonic barcoding (Ji et al., 2019).

Among those demonstrations, a robustly developing technique that leverages optical fiber biosensor has been spurred into the detection of cardiac biomarker and attracted great attentions due to its superiority in structural flexibility, optical alignment-free, high responsivity, resistance to ambient light disturbance, hand-held capability, and network

* Corresponding author.
E-mail address: tguanbo@jnu.edu.cn (B.-O. Guan).

https://doi.org/10.1016/j.bios.2021.113081
Received 3 December 2020; Received in revised form 20 January 2021; Accepted 4 February 2021
Available online 9 February 2021

compatibility for rendering a remote measurement (Wang and Wolfbeis, 2020; Socorro-Leránoz et al., 2019; Guan and Huang, 2019; Yin et al., 2018; Chiavioli et al., 2017; Guo et al., 2017; Pospíšilová et al., 2015). The fiber optic biosensor primarily utilizes the signal wavelength of interest to readout the specific reaction of cardiac biomarkers on the fiber surface (Zhou et al., 2018; Luo et al., 2017; Masson et al., 2004), enabling the potential of point of care testing (POCT) capability, which requires not only the *in-situ* and on-site implementation but also an eligible limit-of-detection (LOD).

In this subset, a deft configuration, that is, microfiber Bragg grating (mFBG), orchestrates the advantages of the fiber Bragg grating and the thinned microfiber together (Zhang et al., 2020; Chen et al., 2019; Xu et al., 2017; Ismaeel et al., 2013; Guan et al., 2013; Tong et al., 2003), facilitating a promising immunoprobe for the cardiac marker detection (Sridevi et al., 2015). First, the extreme compactness with a bulk volume to an order of magnitude of 10^{-14}-10^{-15} m^3 and the self-reflectance signal due to the Bragg condition empowers the mFBG with the potential of endoscopic operation within tiny space, such as the blood capillaries. Second, multiplexing for the individual monitor of patients can be facilitated by networking the tandem of mFBGs with different Bragg wavelengths. More importantly, by virtue of the periodicity of nanoscale and maturity of manufacture (Xiao et al., 2016; Ran et al, 2011, 2012a, 2012b, 2015a), the mFBG allows for the further improvement of the responsivity. For example, the phase-shifted mFBG is capable of checking out the cardiac troponin I protein with a level of as low as 0.03 ng/mL, well beyond the clinical standard of the critical concentration (Liu et al., 2018). After demonstrating the responsivity and specificity of the mFBG based-cardiac marker probe, *in-vivo* and at-patient test is an attractive avenue in which the mFBG can fully exploit its advantages and outweigh its counterparts underlying the feature of time-saving. However, apart from responsivity and specificity, temperature cross-sensitivity is a ubiquitous gap in the avenue that handicapping the pace of mFBG from research to application. Alteration of the body temperature may affect the accuracy of the test, leading to false-positive or negative results. It is thereby urgently tempting to find solutions to eliminate the thermal disturbance in the test.

In this work, we developed and demonstrated a novel strategy exploiting harmonic microfiber Bragg grating to offset the impact of temperature variation during the cardiac biomarker sensing. The harmonic resonances, which were derived by the different overtone orders of the standing waves that formed among the periodic index structure of Bragg grating, allowed for differentiating the specific immune reaction out from the temperature variation. The strategy could overcome the limitations of the conventional temperature-compensating methods, such as the necessities of additional sensing element (Sun et al., 2017) or specialty fiber (Ran et al., 2012a), and the squeeze of the frequency space for multiplexing (Ran et al., 2013). Moreover, the overtone signals could be designed coincidently in the two of the highly commercial and bio-safety wavebands, i.e., the 1 μm and 1.55 μm (Ran et al., 2019), facilitating the long-haul data acquisition that harnesses the signal gain from the industrial ytterbium and erbium-doped fiber amplifiers (Ran et al., 2018), respectively. Most importantly, the proposed scheme yielded an opportunity for us to understand the enhancement of the immune activity at body temperature and shed new light on the rapid diagnosis of AMI.

2. Material and methods

2.1. Materials

The optical fibers were the telecom multimode (62.5/125) and single-mode (SMF-28) silica fibers, which were both purchased from Corning Inc. (USA). 98% sulfuric acid, 30% hydrogen peroxide, hydrochloric acid, sodium chloride, pure ethanol, phosphate buffered saline (PBS), tris buffered saline (TBS, 0.05 mol/L, pH7.4), 25% glutaraldehyde water solution, alphafetoprotein (AFP) antigen, carcinoembryonic antigen-related cell adhesion molecule 5 (CEACAM5), bull serum albumin (BSA) were obtained from Sangon Biotech (Shanghai, China). Human serum was acquired from ZOMANBIO, Ltd. (Beijing, China). 99% 3-aminopropyltriethoxysilane (APTES) was purchased from Sigma-Aldrich (Darmstadt, Germany), Cardiac troponin protein (Recombinant human cardiac troponin I, cTn-I) and corresponding antibody including normal (anti-cTn-I) and fluorescein isothiocyanate -conjugated monoclonal mouse anti-cardiac troponin I (FITC-conjugated anti-cTn-I) were purchased from HyTest Ltd. (Finland). All the chemicals and biological materials were of analytical grade. Deionized (DI) water was used throughout the experiment.

2.2. Fabrication of harmonic microfiber Bragg grating (H-mFBG)

The overall scheme of the device fabrication is shown in Fig. 1. The multimode fiber was tapered to the microfiber with a waist diameter of 3 μm through the flame-heated drawing technique (Ran et al., 2011, 2012b). The diameter of the microfiber was optimally selected in a compromising consideration of outer environment responsivity and insertion loss. The inscription method incorporating a 193 nm excimer laser (Compex 110, Coherent, Inc.) and a phase mask was adopted to imprint the Bragg grating in the microfiber, as depicted in Fig. 1 (a). The repetition rate of the laser was set to 50 Hz. The ultraviolet (UV) energy density was adjusted to 300 mJ/cm^2 per pulse by a cylindrical lens, which was purchased from Thorlabs, Ltd. The pitch of the phase mask (Λ_{pm}) was 1089.21 nm. A supercontinuum light source (SC-5-FC/APC, Wuhan Yangtze Soton Laser Co., Ltd, Wuhan, China) that covers the spectral range from 480 nm to 2200 nm continuously with an output power of 29 dBm was utilized to provide the transmitting input for both target wavelength windows. An optical spectrum analyzer (OSA, Yogokawa, Ltd, AQ6370D) with a resolution limit of 0.01 nm served as the spectral monitor of the reflection of the H-mFBG via a fiber coupler (Thorlabs, Ltd), as shown in Fig. 1(b). The laser exposure was locally immobilized on the waist of the microfiber, lasting for 30 s.

2.3. Principle of H-mFBG

According to the FBG inscription technique utilizing the phase-mask, the incident UV laser is diffracted by the phase mask and then forms a spatially periodic texture that imprints the modulation to the fiber. Ideally, the index modulation would exhibit a uniformly cosine-like contour with the identical modulation amplitude, lying in the interference pattern between the pure ±1 order of diffraction beams. Therefore, the grating period (Λ_g) is half of the Λ_{pm}. The standing wave condition indicates the possible harmonic resonances of the Bragg grating, given by Eq. (1) (Rollison et al., 2012):

$$\lambda(j) = 2N_{eff}\frac{\Lambda_g}{j}, \tag{1}$$

where λ(j) is the reflection wavelength at each harmonic (j = 1,2, 3, …), and N_{eff} stands for the effective index of the fiber. In this case, if the designed Bragg wavelength (λ_{Bragg}), which belongs to the first harmonic resonance, is in the conventional band of 1550 nm, the second harmonic should be found at ~785 nm.

In fact, for a commercial phase mask, however, the ±2 order of diffraction beams can hardly be suppressed completely, resulting in a tailored pattern of the modulation, that is, the "Talbot-type-fringes." The transverse modulation region of the fiber, highly depending on the fiber core diameter, would play a nonnegligible effect on the formation of the grating resonances. As the core diameter is less than half of the Talbot length (Z_T), two modulating contours with a significant contrast of modulation amplitudes interleave in the fiber core, as indicated in Fig. 1 (a). A superstructure grating with a Λ_g that equals to Λ_{pm} ($\Lambda_g = \Lambda_{pm}$) would be established. As a result, λ_{Bragg}, at 1550 nm-band, in the conventional sense, yet mainly relies on the second harmonic resonance (j

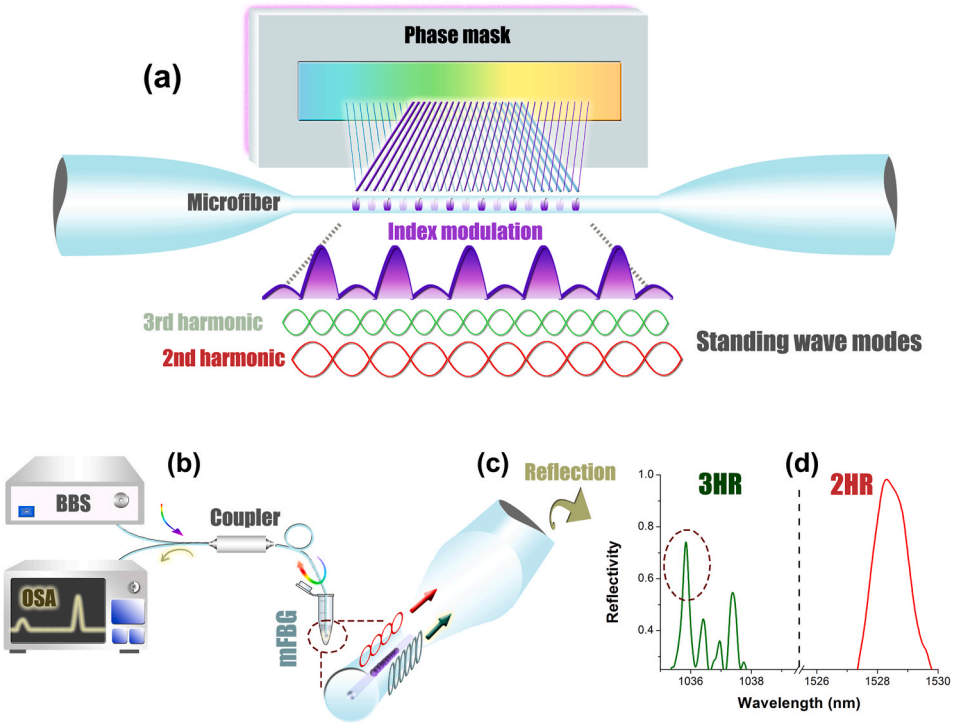

Fig. 1. (a)Schematic of the fabrication of the harmonic microfiber Bragg grating. The 193 nm UV laser was diffracted by the phase mask and then interfered, performing a periodic pattern on the waist of the microfiber. Owing to the participation of the higher order diffractions, the periodic pattern was not uniform but rippled, yielding the periodicity to $\Lambda_{pm.}$ The second and third harmonic standing wave modes oscillated within the pattern, presenting the corresponding resonances at the wavelengths of interest. (b) Diagram of the experimental setup of the interrogation. BBS launched a wide-band light to the mFBG via a coupler. The harmonic resonances were reflected by the mFBG and then delivered to the OSA. (c) Magnified diagram of the mFBG. The grating region oscillated the two harmonic standing wave modes abovementioned and mirrored the correspondent signals. (c) The reflection spectrum of the mFBG acquired by the OSA. Using a phase mask with a pitch of 1089.21 nm, the second and third harmonic resonances were represented by the reflection signals at 1528.4 nm and 1035.8 nm respectively. BBS: broadband light source. mFBG: microfiber Bragg grating. OSA: optical spectral analyzer. 2HR: second harmonic resonance. 3HR: third harmonic resonance.

= 2) (Rollison et al., 2012; Yam et al., 2009). The resonance with respect to the third harmonic (j = 3) is predicted to show at two-third (~1030 nm-band) of λ_{Bragg}, respectively. In our setup, Z_T can be calculated to ~6 μm (Feng et al., 2016a, 2016b; Ran et al., 2015b; Kashyap, 2009), and thus the core of the fiber should be less than 3 μm to guarantee a strong third harmonic reflection at 1030 nm-band. The microfiber, possessing a core diameter of ~1.5 μm that is inferred from the waist diameter, empowers the mFBG to harnesses the harmonic reflections in the two pivotal optical-wavebands (1030 nm and 1550 nm) simultaneously, shown as Fig. 1(c).

Fig. 1(d) displays the reflection spectrum of the mFBG in these two bands. The second harmonic resonance (2HR) presented a higher reflectivity of 99.5% with a peak wavelength of 1528.4 nm. At 1030 nm-band, there were multiple reflections probably due to the intermodal interference with respect to the multimode operation of the system at a great shorter wavelength. Nevertheless, the strongest signal, as indicated, with the reflectivity over 78% of the third harmonic resonance (3HR) was selected for the interrogation, locating at 1035.8 nm.

2.4. Functionalization of H-mFBG

For granting the H-mFBG with the specificity aiming at the cTn-I protein, we need to immobilize the cTn-I antibody on the surface of the fiber. The covalent bonding method was adopted to enable a stable configuration (Regan et al., 2018). The functionalization of the PS-mFBG probe was charted as the procedures described below. It was worth noting that the H-mFBG probe underwent a 5 min-rinsing of DI water for wiping out the residual molecules and stabilized at the end of each procedure.

Fig. 2(a) recorded the spectral response of 2HR regarding to the peak wavelength during the procedures of functionalization from (2) to (4) ab initio. Regarding that the wavelength of 2HR presented no significant

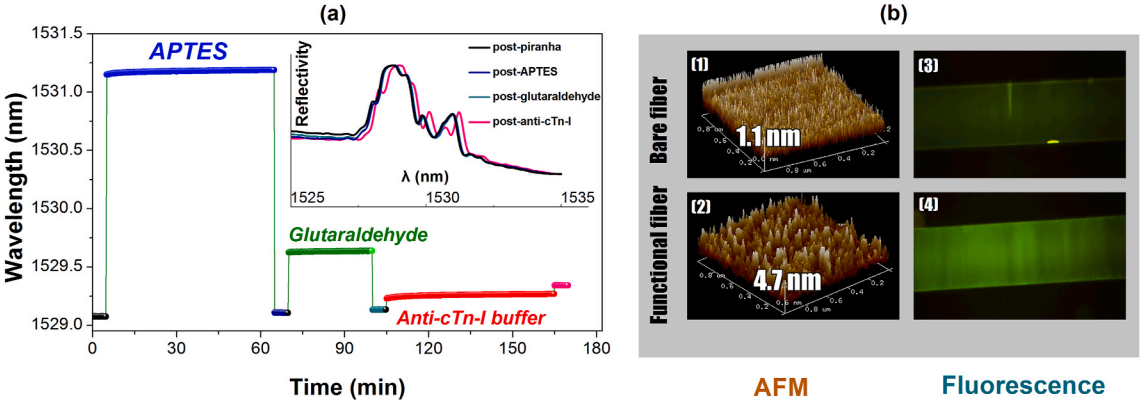

Fig. 2. (a) Wavelength variation of the 2HR during the three critical phases, that is, silanization, cross linking, and functionalization of the functionalized process. The wavelength at the end of each phase, in contrast with the beginning, indicated the alteration of the surface state. (b) Comparison chart on the morphology of the fiber surface between the bare fiber (up) and functionalized fiber anchored with anti-cTn-I (down) using AFM imaging (left) and fluorescence imaging (right). The functionalized fiber possessed not only a higher roughness but also a brighter fluorescence of the surface. APTES: 3-aminopropyltriethoxysilane; cTn-I: cardiac troponin-I; AFM: atomic force microscope.

difference in the piranha treatment because there was no alteration of the surface feature, the dynamic process was started from the DI water rinsing after the hydroxylation procedure.

From the DI water to the APTES procedure (2), an abrupt jump-up over 1 nm of the Bragg wavelength could be observed due to the higher RI of the APTES ethanol solution. At the end of the procedure, yet the value of the wavelength jumped downward in the second DI water rinsing step. The difference of Bragg wavelength between these two DI water rinsing steps was ~30 p.m., indicating the successful silanization of the silica surface. As procedure (3), the glutaraldehyde PBS solution offered a higher RI as well, yet the scale was different. The Bragg wavelength shifting stair was counted to ~0.5 nm. Afterward, in the DI water rinsing, the actual wavelength shift of this procedure could be measured to ~30 p.m., denoting the implementation of the cross-linking functionality. During procedure (4), we could explore a continuous red-shifting of the Bragg wavelength, which reflected the process of the cTn-I antibody bonding, to a considerable quantity of 0.21 nm ultimately.

For validating the functionalization, two kinds of imaging approaches, the atomic force microscopy (AFM) and immunofluorescent microscopy, were employed. Fig. 2(b1 and b2) conveyed the distinct contrast of the surface feature between the H-mFBGs that without and with the anti-cTn-I-functional layer using AFM. The functionalized probe was imaged after a 24-h drying process. It could be found that the functional probe had a larger non-uniform surface with a higher perturbation ratio than the bare one, implying that the functional layer was glued on the surface. Furthermore, the FITC-conjugated anti-cTn-I was utilized to render the fluorescent images. As shown in the fluorescence-microscopic image in Fig. 2(b3 and b4), compared with the bare fiber, the functional fiber exhibited a brighter profile shedding the green light, which was excited by a microscope-integrated 455 nm laser. Therefore, it could also be nailed down that the cTn-I protein identification functionality was successfully bestowed upon the sensor.

$$\begin{pmatrix} \Delta RI(RIU) \\ \Delta T(^{\circ}C) \end{pmatrix} = \begin{pmatrix} 59.6 & 0.0036 \\ 10.5 & 0.0057 \end{pmatrix}^{-1} \begin{pmatrix} \Delta\lambda_{2HR} \\ \Delta\lambda_{3HR} \end{pmatrix} \quad (2)$$

3. Results and discussion

3.1. Sensor characterization

For achieving the aim of acceleration of the immunoreaction speed and shortening of the test time, the ideal method is to conduct the test on the human body with an optimal temperature of 37 ^{O}C, in which the maximum activities of the proteins can be spurred. However, temperature fluctuation often occurs individually, sabotaging the precise test results. Thus, it necessitates the temperature-discriminating functionality of the sensor, especially for the use of the optical fiber, which possesses a substantially thermo-optical effect. The RI-temperature dual sensing capability of the proposed functional H-mFBG was investigated. At first, the RI response characteristic of the probe was studied by immersing the grating region into the sodium chloride solution. The RI of the calibrating solution could be tuned, ranging from 1.33 to 1.38, by

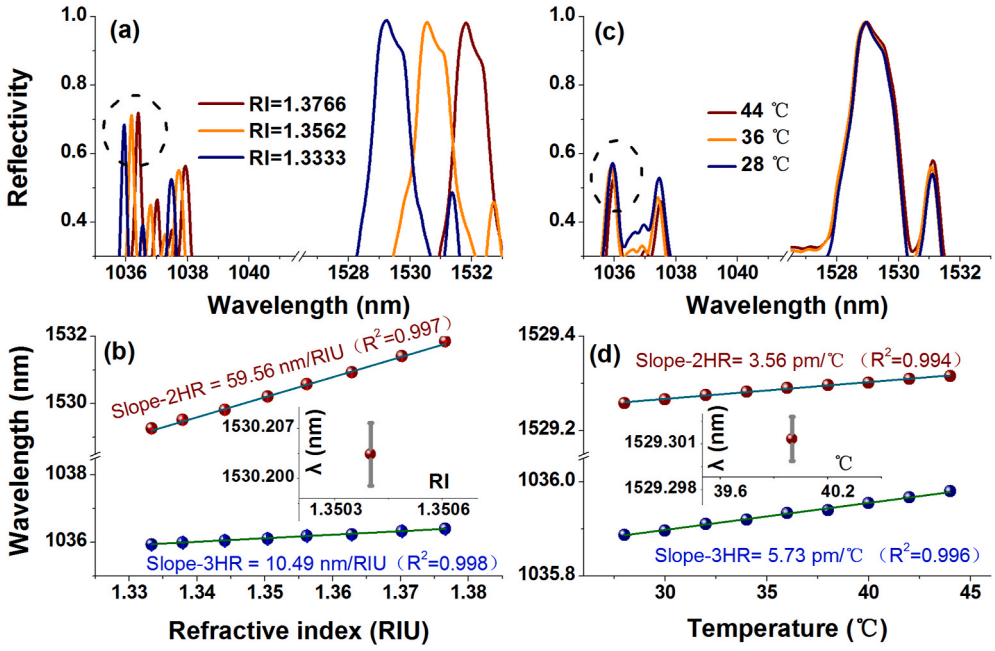

Fig. 3. The functionalized H-mFBG:(a) spectral variation according to the change of ambient RI. (b) Calibration curves of 2HR and 3HR with respect to ambient RI. Inset: magnified point of measurement at the RI of 1.35. (c) spectral variation according to the change of ambient water temperature; (d) Calibration curves of 2HR and 3HR with respect to ambient water temperature. Inset: magnified point of measurement at the temperature of 40 ^{O}C. The dashed circles in (a) and (c) highlighted the peak for data acquisition of the 3HR. Error bars indicated that the results were obtained by independent measurements (N = 3). R^2: regression factor.

(1) Hydroxylation. The H-mFBG probe was inserted and stood for 1 h in the piranha solution prepared by hybridizing the 98% sulfuric acid and 30% hydrogen peroxide with a volume ratio of 3:1 for taking the hydroxyl on the silica surface. After the 5-min rinsing of DI water, an additional three-time ethanol solution washing was required against the hydrolyzation of silanizing solvent in the next step.
(2) Silanization. The probe was immersed into a 5% APTES ethanol solution for 1 h to conduct the reaction to generate amino-group on the surface.
(3) Cross-link. The probe was dipped into the 5% glutaraldehyde PBS solution for 30 min. The glutaraldehyde would attach on the silica surface by virtue of its one of the aldehyde groups that bond with the amino-group, leaving another free aldehyde group on standby.
(4) Functionalization. The probe was immersed into the anti-cTn-I spiked PBS solution (10 μg/mL) for 30 min. The solution was prepared by diluting the anti-cTn-I into the PBS with a pH of 7.4. The cTn-I antibody was immobilized through binding the aldehyde group above-mentioned utilizing the amino-group, and thus a monolayer of anti-cTn-I was formed on the fiber surface.
(5) Blocking. The BSA solution was used to rinse the probe for 30 min to occupy and block the unbind aldehyde groups on the surface for the aim of eliminating the non-specific binding.

simply changing the concentration of the solute. Fig. 3(a) elaborates on the spectral change of the two harmonic resonances in accordance with the alteration of liquid RI. It could be seen that 2HR presented a more significant redshift than 3HR. By the quantitative analysis of the response curve, illustrated as Fig. 3(b), the RI linear-responsivity of 3HR and 2HR could be obtained to 10.5 nm/RIU and 59.6 nm/RIU, respectively. The difference ratio of linear-responsivity, described as (Resp. 2HR-Resp. 3HR)/Resp. 2HR, between the two resonances, was 82.4%. Second, the temperature response was monitored by inserting the functionalized H-mFBG into deionized water whose temperature could be operated from 28 ^{O}C to 44 ^{O}C by a heating plate. According to Fig. 3 (c), both resonances moved slightly to the longer wavelength with the enhancement of the water temperature. The wavelength shifts could be seen obviously in the transmission spectrum, as shown in Fig. S1. Fig. 3 (d) quantitatively illustrated the temperature linear-responsivity of 3HR and 2HR as 0.0057 nm/^{O}C and 0.0036 nm/^{O}C, respectively, exhibiting a difference ratio of −58%. The lower temperature linear-responsivity in comparison with the conventional FBG sensors could be attributed to the decrease of the water RI, which offset the positive response of resonances, during the heating, 3HR, holding a distinct response curve with respect to the 2HR, could facilitate the simultaneous measurement of RI and temperature (or temperature compensation). Therefore, the change of both parameters could be acquired at the same time through interrogating the wavelength shifts of 3HR and 2HR and calculating the matrix of Eq (2) that derived from the response curves:

3.2. Calibration curve and specificity of the cTn-I sensor

The lyophilized cTn-I protein was reconstituted to different concentrations ranging from 1 ng/mL to 1000 ng/mL using the TBS buffer. Firstly, the response curve of the H-mFBG immunosensor was plotted by measuring those calibrated cTn-I samples. A high-resolution optical spectrum analyzer (BOSA-light, Argon Photonics, Ltd, Spain) with a spectral resolution of 0.1 p.m. was utilized to capture the tiny change that associated to the immunobinding of cTn-I. Three independent tests were repeated at each sample. It should be mentioned that, in order to eliminate the additional error that was introduced by using the different fiber Bragg grating devices, it is preferred to recycle the same fundamental harmonic microfiber Bragg grating device in each independent test. Since the antibody was occupied by the antigen and the bond was not easy to disassemble, we utilize the piranha solution to wash the bioprobe for 30 min to remove the entire functional layer on the surface after each test, as shown in Fig. S2, (Sun et al., 2015; Liang et al., 2018; Liu et al., 2018). The fundamental harmonic microfiber Bragg grating device was restored with the bare silica surface and then experienced a new modification process to refabricate the biosensor (as shown in Fig. S3) for conducting a new cTn-I test, following the functionalization procedures ab initio, which were described in Section 2.4.

The response curve of the 2HR regarding the alteration of the cTn-I buffer solution with different concentrations, was depicted in Fig. 4 (a). The total response time for each detection was 60 min. A log-linearly calibrated curve could be drawn, presenting a linear slope of 0.0152 nm/(ng/mL) ranging from 3 ng/mL to 1 μg/mL. By logging the long-term variation of the signal at blank sample (cTn-I = 0 ng/mL), the wavelength drift ($\overline{\Delta\lambda_{blank}}$) and standard deviation (σ) were obtained to 0.0035 nm and 0.0042 nm, respectively. By calculating the limit of detection (LOD) from Eq. (3), defined by (Chiavioli et al., 2017).where f^{-1} denotes the inverse of the fitting function. The LOD of this H-mFBG immnunosensor could reach 13.5 ng/mL. The small effective wavelength shift of 0.016 nm in accordance with the LOD further features the importance of enrolling the temperature compensational technique in cTn-I sensing.

In order to prove the specificity (defined as the sensor's ability to be sensitive to a specific measurand for biosensors) of the probe, two kinds

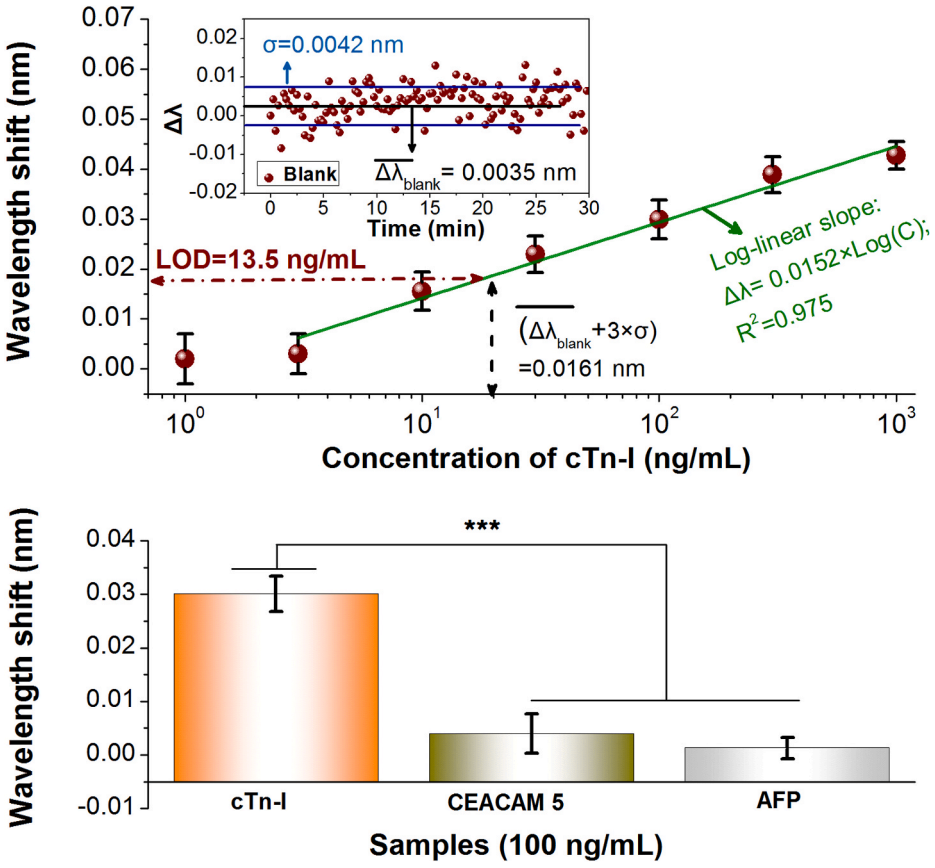

Fig. 4. (a)Response and calibration curves of the 2HR of the H-mFBG in sensing cTn-I TBS buffer with different concentrations ranging from 1 ng/mL to 1000 ng/mL (b)Measurement of the biomolecules of specificity (cTn-I) and non-specificity (CEACAM 5 and AFP) in the TBS buffer with the same concentration (0.1 μg/mL) using the H-mFBG bioprobe. ***indicated the hypothesis testing with $p < 0.01$ (0.0065), showing a great significance of the test towards specific sample group. Δλ: wavelength shift; σ: standard deviation; LOD = limit of detection; CEACAM 5: carcinoembryonic antigen-related cell adhesion molecule 5; AFP: alphafetoprotein antigen. Error bars indicated that the results were obtained by independent measurements (N = 3).

of non-specific proteins, CEACAM 5 and AFP, were employed as the control analytes. The three kinds of solution were prepared at the same concentration of 0.1 μg/mL. Fig. 4(a) recorded the responses of the 2HR regarding those kinds of solutions. The typical kinetic response curves were shown in Fig. S4. Larger error bars, which are probably due to the activity of the target antigen and the concentration deviation in the independent tests, could be seen in the results of the specific sensing group; Nevertheless, a great statistical significance (statistical hypothesis: $p < 0.01$) between target groups and control groups could still manifest the high specificity of the sensing probe aiming at the cTn-I protein.

3.3. Acceleration of cTn-I test

In-vivo and direct detection of the cardiac biomarker at patient not only waives the spatial turn-around process but also boosts the immune activity at the human body temperature, tremendously enhancing the test efficiency, which is essential for the instant diagnosis and prognosis and thereby saving lives. As a consequence, the temperature discernibility is highly demanded in the fiber optic-based cardiac biomarker biosensors. To this end, the cTn-I fast-test experiment was preliminarily performed by using the human serum to mimic realistic conditions for demonstrating its POC and *in-vivo* diagnosis potential. The H-mFBG probe was tested by the 0.1 μg/mL cTn-I serum samples in two scenarios with different temperatures, i.e., the room temperature (25 ^{O}C) and human body temperature (37 ^{O}C). The serum matrices were used as the original concentration as obtained without further diluting. 2HR and 3HR of the H-mFBG functional probe were involved to offset the influence of the environment temperature. The responses of the two resonances were recorded in Fig. 5(a) with respect to the two temperature scenarios. The larger responses in the serum compared with TBS buffer at room temperature were probably due to the bonding of some unknown biomolecules on the fiber surface. An updated calibration is perhaps required as the sensor comes into the real application scenario for testing the original blood. Nevertheless, the distinct responses between 2HR and 3HR still allowed for monitoring the temperature during the cTn-I test. The resonances of the probe presented larger redshifts at the body temperature, indicating that the influence of the temperature was exerted in the detection. By monitoring the two resonant signals, the comparison of the dynamic responses at the different temperatures was uncovered in Fig. 5(b). At 37 ^{O}C, the two resonances exhibited more significant time-dependent responses. It worth noting that the kinetic curve of 37 ^{O}C included a heating process started from 25 ^{O}C. The impact of the heating process acted on the kinetic curve needed to be understood for further closing to the sensing application in reality. A normal FBG, which showed no response to RI, written in the single-mode fiber was utilized as a thermal sensor to *in-situ* and real-time acquisition of the serum temperature during heating (Hill and Meltz, 1997). The temperature linear-responsivity of the FBG was 10 p.m./^{O}C, seen as the inset of Fig. 5(c). During different heating processes that targeting the stabilized temperature of 34 ^{O}C, 36 ^{O}C, and 40 ^{O}C, different wavelength shifting could be observed correspondingly, in Fig. 5, although, the temperature elevating intervals were all about 5 min. Therefore, the evolution of the curve after 5 min was assumed to represent the phase of the specific immune reaction at a stabilized temperature of 37 ^{O}C. As mentioned in *3.1*, the impact of temperature that acted on the 2HR's wavelength-shift could be eliminated via subtracting the weighed wavelength-shift of 3HR, which was derived by solving the matrix equation in Eq. (2). Therefore, by processing the data recorded in Fig. 5 (b), the kinetic responses of 2HR with the absolute alteration of RI, which was attributed by the cTn-I protein binding, could be obtained at different temperature status, as portrayed in Fig. 5(d). The effective wavelength-shift of the 2HR after 1-h testing at room temperature is ~0.03 nm. At body temperature, by contrast, the rate and amplitude of the response were significantly elevated due to the strengthening of the enzymatic activity. The 1-h reaction yielded a total wavelength shift of the resonance to ~0.054 nm. Furthermore, the body temperature test possessed a considerably shorter response time to 25 min regarding the

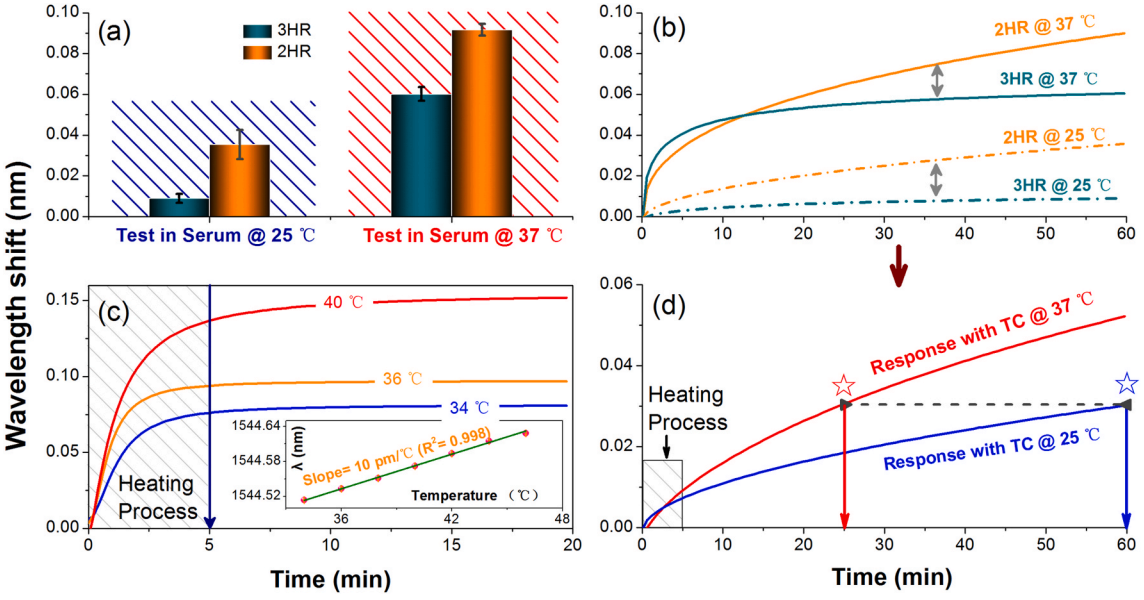

Fig. 5. (a) Comparison diagram of the responsivity of the cTn-I sensor between the ambient temperatures of 25 ^{O}C and 37 ^{O}C. The target samples were the same of the serum spiked with cTn-I to 0.1 μg/mL. (b) Kinetic responses of the harmonic resonances in sensing cTn-I at different temperatures (25 ^{O}C and 37 ^{O}C). (c) Kinetic responses of a conventional single mode fiber Bragg grating to characterize the time of response during the water-bathing from 25 ^{O}C to different designated temperatures. A 5-min process could be observed in all of the measurements. Inset: the calibration curve of the single mode fiber Bragg grating responding to the temperature. (d) Kinetics of the pure response, derived by subtracting the influence of the temperature via solving Eq. (1), of the H-mFBG to the cTn-I at different temperatures. Error bars indicated that the results were obtained by independent measurements (N = 3). TC: temperature compensation.

$$X_{LOD} = f^{-1}(\overline{y_{black}} + 3\sigma) \quad (3)$$

wavelength shift obtained by the 1-h room temperature test (0.03 nm). It could be envisioned that, with the aid of cutting the time-consume by more than a half, the total turn-around-time (TAT) of the cTn-I test could be significantly shortened by virtue of the manipulation at body temperature. More importantly, the duet of the harmonic resonances in sensing allowed for monitoring the cTn-I level on-patient without being subjected to the temperature cross-sensitivity, featuring the potential of an even faster test that avoids the complex procedures of sample transfer and storage. The proposed probe can be one of the POCT approaches without suffering from the temperature fluctuation, such as optofluidic laser (Yang et al., 2019, 2020) and paper-based fluorescence device (Luo et al., 2020).

4. Conclusion

A novel mFBG probe is proposed for the label-free and high-efficient test of the cardiac biomarkers, for example, the cTn-I. The mFBG orchestrates the harmonic reflections to eliminate the temperature cross talk. In addition, the harmonic reflections locate at 1 μm and 1.55 μm wavebands, respectively, that can harvest gain from commercial fiber optical amplifiers, enabling the utility of point-of-care tests at patients. Furthermore, the probe can scrutinize the kinetic, which involves the alteration of the ambient temperature, and effectively elicit the pure immune reaction for understanding the vitality of the biomolecules. It is explored that the reaction rate would be significantly elevated at the human body temperature (37 ^{O}C), in contrast to the room temperature (25 ^{O}C), due to the enhancement of biomolecular activity in the optimum condition. The scheme offers a new route to minimize the time-consuming of the cardiac biomarker test through the build-in fiber photothermal management technique or even patient-beside determination. Future works may involve the responsivity improvement, which is essential for early screening. Several techniques, such as the phase-shifted Bragg grating (Liu et al., 2018) and optimized thinner fiber Bragg grating, can be invested in this scheme to hit the cut-off diagnostic criteria. Besides, a steady protection configuration is required to keep the sensor out of damage. Several antigen unbinding methods, such as sodium dodecyl sulfate rinsing, can be involved to facilitate the sensor reconfiguration (Chiavaioli et al., 2018). More importantly, the highly commercial fiber and grating used in this work can also sustain the cost reduction in fabrication for disposable usage, which is more preferred in the at-patient test. In the future investigation on the assay of the real samples from the patients, the diagnostic tests exploiting the “sensitivity (%)” (probability that a sample tests “positive” regarding the patient has the disease) and “specificity (%)” (the probability that a test reflects a negative result regarding the patient does not have the disease) will be carried out for evaluating the performance of the biosensor in the fast screening and diagnosis (Trevethan, 2017). The demonstration and scientific findings in this work provide guidance for future attempts to achieve fast and in-vivo tests for acute cardiac disease.

CRediT authorship contribution statement

Yang Ran: Conceptualization, Methodology, Writing - original draft, Writing - review & editing, Funding acquisition. **Junqiu Long:** Methodology, Investigation, Writing - original draft. **Zhiyuan Xu:** Investigation. **Yi Yin:** Investigation. **Deming Hu:** Validation. **Xueting Long:** Validation. **Yongkang Zhang:** Validation. **Lili Liang:** Methodology, Funding acquisition. **Hao Liang:** Writing - original draft, Funding acquisition. **Bai-Ou Guan:** Conceptualization, Writing - review & editing, Supervision, Funding acquisition.

Declaration of competing interest

The authors declare no conflict of interest.

Acknowledgement

This work was supported by National Natural Science Foundation of China (Grant No. 61775082, U1701268, 61805106, 61675091), the Local Innovative and Research Teams Project of Guangdong Pearl River Talents Program (Grant No. 2019BT02X105), Guangdong Natural Science Foundation (Grant No. 2018A030313677), the Fundamental Research Funds for the Central Universities.

Appendix A. Supplementary data

Supplementary data to this article can be found online at https://doi.org/10.1016/j.bios.2021.113081.

References

Agafonova, L.E., Shumyantseva, V.V., Archakov, A.I., 2014. Chem. Phys. Lett. 604, 5–9.
Chen, J., Li, D., Xu, F., 2019. J. Lightwave Technol. 37, 2577–2589.
Chiavaioli, F., Gouveia, A.J.C., Jorge, A.S.P., Baldini, F., 2017. Biosensors 7 (2).
Chiavaioli, F., Zubiate, P., Del Villar, I., Zamarreño, C.R., Giannetti, A., Tombelli, S., Trono, C., Arregui, F.J., Matias, I.R., Baldini, F., 2018. ACS Sens. 3 (5), 936–943.
Diware, M.S., Cho, H.M., Chegal, W., Cho, Y.J., Kim, D.S., O, S.W., Kim, K.-S., Paek, S.-H., 2017. Biosens. Bioelectron. 87, 242–248.
El-Said, W.A., Fouad, D.M., El-Safty, S.A., 2016. Sensor. Actuator. B Chem. 228, 401–409.
Fan, X., White, I.M., Shopova, S.I., Zhu, H., Suter, J.D., Sun, Y., 2008. Anal. Chim. Acta 620, 8–26.
Fathil, M.F.M., Md Arshad, M.K., Gopinath, S.C.B., Hashim, U., Adzhri, R., Ayub, R.M., Ruslinda, A.R., Nuzaihan, M.N.M., Azman, A.H., Zaki, M., Tang, T.H., 2015. Biosens. Bioelectron. 70, 209–220.
Feng, F.-R., Liu, T., Xiao, P., Ran, Y., Liang, H., Jin, L., Guan, B.-O., 2016a. Opt. Lett. 41, 4999–5002.
Feng, F.-R., Ran, Y., Liang, Y.-Z., Gao, S., Feng, Y.-H., Jin, L., Guan, B.-O., 2016b. Opt. Lett. 41, 2470–2473.
Guan, B.-O., Huang, Y., 2019. J. Lightwave Technol. 37, 2616–2622.
Guan, B.O., Li, J., Jin, L., Ran, Y., 2013. Opt. Fiber Technol. 19, 793–801.
Guo, T., González-Vila, Á., Loyez, M., Caucheteur, C., 2017. Sensors 17, 1–20.
Hill, K.O., Meltz, G., 1997. J. Lightwave Technol. 15, 1263–1276.
Ismaeel, R., Lee, T., Ding, M., Belal, M., Brambilla, G., 2013. Laser Photon. Rev. 7, 350–384.
Ji, J., Lu, W., Zhu, Y., Jin, H., Yao, Y., Zhang, H., Zhao, Y., 2019. ACS Sens. 4, 1384–1390.
Kashyap, R., 2009. Fiber Bragg Gratings. Academic press.
Liang, L., Jin, L., Ran, Y., Sun, L.-P., Guan, B.-O., 2018. Anal. Chem. 90, 10851–10857.
Liu, T., Liang, L.-L., Xiao, P., Sun, L.-P., Huang, Y.-Y., Ran, Y., Jin, L., Guan, B.-O., 2018. Biosens. Bioelectron. 100, 155–160.
Luo, B., Wu, S., Zhang, Z., Zou, W., Shi, S., Zhao, M., Zhong, N., Liu, Y., Zou, X., Wang, L., Chai, W., Hu, C., Zhang, L., 2017. Biomed. Optic Express 8, 57–67.
Luo, Z., Lv, T., Zhu, K., Li, Y., Wang, L., Gooding, J.J., Liu, G., Liu, B., 2020. Angew. Chem. Int. Ed. 59 (8), 3131–3136.
Mahajan, V.S., Jarolim, P., 2011. Circulation 124, 2350–2354.
Masson, J.F., Obando, L., Beaudoin, S., Booksh, K., 2004. Talanta 62, 865–870.
Mattos, A.B., Freitas, T.A., Silva, V.L., Dutra, R.F., 2012. Sensor. Actuator. B Chem. 161 (1), 439–446.
Mohammed, M.I., Desmulliez, M.P.Y., 2011. Lab Chip 11, 569–595.
Pawula, M., Altintas, Z., Tothill, I.E., 2016. Talanta 146, 823–830.
Pospíšilová, M., Kuncová, G., Trögl, J., 2015. Sensors 15, 25208–25259.
Qureshi, A., Gurbuz, Y., Niazi, J.H., 2012. Sensor. Actuator. B Chem. 171–172, 62–76.
Ran, Y., Long, J., Xu, Z., Hu, D., Guan, B.-O., 2019. Opt. Lett. 44, 3186–3189.
Ran, Y., Xu, Z., Feng, F., Xiao, P., Liang, Y., Jin, L., Guan, B.-O., 2018. Opt. Lett. 43, 2787–2790.
Ran, Y., Jin, L., Gao, S., Sun, L.P., Huang, Y.Y., Li, J., Guan, B.O., 2015. Opt. Lett. 40, 3802–3805.
Ran, Y., Jin, L., Sun, L.P., Li, J., Guan, B.O., 2013. IEEE Photon. J. 5, 7100208.
Ran, Y., Jin, L., Sun, L.P., Li, J., Guan, B.O., 2012a. Opt. Lett. 37, 2649–2651.
Ran, Y., Jin, L., Tan, Y.N., Sun, L.P., Li, J., Guan, B.O., 2012b. IEEE Photon. J. 4, 181–186.
Ran, Y., Tan, Y.N., Sun, L.P., Gao, S., Li, J., Jin, L., Guan, B.O., 2011. Optic Express 19, 18577–18583.
Regan, B., O'Kennedy, R., Collins, D., 2018. Biosensors 8 (4), 1–32.
Rollinson, C.M., Wade, S.A., Kouskousis, B.P., Kitcher, D.J., Baxter, G.W., Collins, S.F., 2012. J. Opt. Soc. Am. A 29, 1259–1268.
Saliminasab, M., Bahrampour, A., Zandi, M.H., 2012. J. Optics-UK 14, 1–7.
Socorro-Leránoz, A.B., Santano, D., Del Villar, I., Matias, I.R., 2019. Biosens. Bioelectron. X 1, 100015.
Sridevi, S., Vasu, K.S., Asokan, S., Sood, A.K., 2015. Biosens. Bioelectron. 65, 251–256.
Sun, D., Ran, Y., Wang, G., 2017. Sensors 17, 1–8.
Sun, P., Liu, G., Lv, D., Dong, X., Wu, J., Wang, D., 2015. RSC Adv. 5 (65), 52916–52925.
Tang, L., Casas, J., 2014. Biosens. Bioelectron. 61, 70–75.
Thygesen, K., Alpert, J.S., White, H.D., Jaffe, A.S., Katus, H.A., Apple, F.S., Lindahl, B., Morrow, D.A., Chaitman, B.R., Clemmensen, P.M., Johanson, P., Hod, H.,

Underwood, R., Bax, J.J., Bonow, R.O., Pinto, F., Gibbons, R.J., Fox, K.A., Atar, D., Newby, L.K., Galvani, M., Hamm, C.W., Uretsky, B.F., Steg, P.G., Wijns, W., Bassand, J.-P., Menasche, P., Ravkilde, J., Ohman, E.M., Antman, E.M., Wallentin, L. C., Armstrong, P.W., Simoons, M.L., Januzzi, J.L., Nieminen, M.S., Gheorghiade, M., Filippatos, G., Luepker, R.V., Fortmann, S.P., Rosamond, W.D., Levy, D., Wood, D., Smith, S.C., Hu, D., Lopez-Sendon, J.-L., Robertson, R.M., Weaver, D., Tendera, M., Bove, A.A., Parkhomenko, A.N., Vasilieva, E.J., Mendis, S., 2012. J. Am. Coll. Cardiol. 60, 1581–1598.

Tong, L., Gattass, R.R., Ashcom, J.B., He, S., Lou, J., Shen, M., Maxwell, I., Mazur, E., 2003. Nature 426, 816–819.

Trevethan, R., 2017. Sensitivity, specificity, and predictive values: foundations, pliabilities, and pitfalls in research and practice. Front Public Health 5, 307-307.

Tripoliti, E.E., Ioannidou, P., Toumpaniaris, P., Rammos, A., Pacitto, D., Lourme, J., Goletsis, Y., Naka, K.K., Errachid, A., Fotiadis, D.I.I., 2020. IEEE Rev. Biomed. Eng. 3, 17–31.

Tuteja, S.K., Chen, R., Kukkar, M., Song, C.K., Mutreja, R., Singh, S., Paul, A.K., Lee, H., Kim, K.-H., Deep, A., Suri, C.R., 2016. Biosens. Bioelectron. 86, 548–556.

Wang, X., Wolfbeis, O.S., 2020. Anal. Chem. 92, 397–430.

White, H.D., Chew, D.P., 2008. Lancet 372, 570–584.

WHO, 2015. Cardiovascular Diseases. World Health Organization. http://www.who.int/mediacentre/factsheets/fs317/en/.

Wu, Q., Sun, Y., Zhang, D., Li, S., Zhang, Y., Ma, P., Yu, Y., Wang, X., Song, D., 2017. Biosens. Bioelectron. 96, 288–293.

Xiao, P., Liu, T., Feng, F.R., Sun, L.P., Liang, H., Ran, Y., Jin, L., Guan, B.O., 2016. Optic Express 24, 29749–29759.

Xu, Y., Lu, P., Chen, L., Bao, X., 2017. Fibers 5, 1–42.

Yam, S.P., Brodzeli, Z., Kouskousis, B.P., Rollinson, C.M., Wade, S.A., Baxter, G.W., Collins, S.F., 2009. Opt. Lett. 34, 2021–2023.

Yang, X., Luo, Y., Liu, Y., Gong, C., Wang, Y., Rao, Y.-J., Peng, G.-D., Gong, Y., 2020. Lab Chip 20 (5), 923–930.

Yang, X., Shu, W., Wang, Y., Gong, Y., Gong, C., Chen, Q., Tan, X., Peng, G.-D., Fan, X., Rao, Y.-J., 2019. Biosens. Bioelectron. 131, 60–66.

Yin, M.-j., Gu, B., An, Q.-F., Yang, C., Guan, Y.L., Yong, K.-T., 2018. Coord. Chem. Rev. 376, 348–392.

Zhang, B., Morales, A.W., Peterson, R., Tang, L., Ye, J.Y., 2014. Biosens. Bioelectron. 58, 107–113.

Zhang, D., Huang, L., Liu, B., Ni, H., Sun, L., Su, E., Chen, H., Gu, Z., Zhao, X., 2018a. Biosens. Bioelectron. 106, 204–211.

Zhang, D., Huang, L., Liu, B., Su, E., Chen, H.-Y., Gu, Z., Zhao, X., 2018b. Sensor. Actuator. B Chem. 277, 502–509.

Zhang, L., Tang, Y., Tong, L., 2020. iScience 23, 100810.

Zhou, W., Li, K., Wei, Y., Hao, P., Chi, M., Liu, Y., Wu, Y., 2018. Biosens. Bioelectron. 106, 99–104.